

UCLA

UCLA Previously Published Works

Title

Ambient methane functionalization initiated by electrochemical oxidation of a vanadium (V)-oxo dimer.

Permalink

<https://escholarship.org/uc/item/04t5s5m8>

Journal

Nature communications, 11(1)

ISSN

2041-1723

Authors

Deng, Jiao

Lin, Sheng-Chih

Fuller, Jack

et al.

Publication Date

2020-07-01

DOI



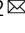

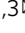


10.1038/s41467-020-17494-w

Copyright Information

This work is made available under the terms of a Creative Commons Attribution License, available at <https://creativecommons.org/licenses/by/4.0/>

Peer reviewed

Ambient methane functionalization initiated by electrochemical oxidation of a vanadium (V)-oxo dimer

Jiao Deng¹, Sheng-Chih Lin², Jack Fuller III ¹, Jesus A. Iñiguez¹, Danlei Xiang¹, Di Yang¹, Gary Chan¹, Hao Ming Chen ², Anastassia N. Alexandrova ^{1,3} & Chong Liu ¹

The abundant yet widely distributed methane resources require efficient conversion of methane into liquid chemicals, whereas an ambient selective process with minimal infrastructure support remains to be demonstrated. Here we report selective electrochemical oxidation of CH₄ to methyl bisulfate (CH₃OSO₃H) at ambient pressure and room temperature with a molecular catalyst of vanadium (V)-oxo dimer. This water-tolerant, earth-abundant catalyst possesses a low activation energy (10.8 kcal mol⁻¹) and a high turnover frequency (483 and 1336 hr⁻¹ at 1-bar and 3-bar pure CH₄, respectively). The catalytic system electrochemically converts natural gas mixture into liquid products under ambient conditions over 240 h with a Faradaic efficiency of 90% and turnover numbers exceeding 100,000. This tentatively proposed mechanism is applicable to other d⁰ early transition metal species and represents a new scalable approach that helps mitigate the flaring or direct emission of natural gas at remote locations.

¹Department of Chemistry and Biochemistry, University of California, Los Angeles, Los Angeles, CA 90095, USA. ²Department of Chemistry, National Taiwan University, Taipei 10617, Taiwan. ³California NanoSystems Institute, Los Angeles, CA 90095, USA. ✉email: haomingchen@ntu.edu.tw; ana@chem.ucla.edu; chongliu@chem.ucla.edu

The wide geological distribution of natural gas resources leads to an undesirable loss of methane (CH_4) especially at remote locations via flaring or direct emission into the atmosphere^{1,2}. One possible strategy to mitigate such an issue is to convert CH_4 into liquid chemicals at the source of emission under ambient condition with minimal reliance on an industrial infrastructure². Fundamentally, this catalytic conversion requires low activation energy and high reactivity, in order to accommodate the low thermal energy and partial pressure of CH_4 substrate at ambient condition. Existing approaches of CH_4 functionalization usually operated at high pressure and/or elevated temperature^{3–16}, involve metal-catalyzed reactions^{3–7}, superacid-based activation¹⁷, or catalysis based on peroxy species for a free-radical chain mechanism^{8–10}. For the metal-catalyzed reactions reported by Periana and others (Fig. 1a)^{3–6}, electrophilic activation of CH_4 is followed by an oxidation process that regenerates the metal active sites, mostly precious metals including Pt and Pd. Yet, in ambient conditions, the reactivities of these electrophilic metal species seem insufficient to activate CH_4 . In the approaches based on radical chain mechanism (Fig. 1b)^{8–10}, initiators including peroxy species yield oxygen radicals that activate CH_4 at room temperature with low activation energies¹⁸. But it is uneasy to achieve a sustained, selective catalytic process that generates and replenishes radical species. The challenge of balancing the reactivity and regeneration of active species call for an alternative approach for ambient CH_4 functionalization.

We propose that a controlled electrochemical generation of oxygen radicals is capable to address the above-mentioned challenge, as electrochemical redox process provides a sustained method of replenishing radical species at ambient conditions without sacrificing their high reactivities^{19,20}. While d^0 early transition metal centers are not known to be directly oxidizable, we accidentally found that electrochemical oxidation of d^0 early transition metal-oxo species in 68–98% H_2SO_4 yields cation

radicals on the sulfonic ligand that selectively activate CH_4 at ambient pressure and room temperature (Fig. 1c). Here, we report d^0 vanadium (V)-oxo dimer ($\text{V}_2^{\text{V,V}}$, **1**)²¹ as the model catalyst for mechanistic understanding (Fig. 1d). As the tentative turnover-limiting step (TLS) uncommon for homogenous electrocatalysis, an electrochemical one-electron removal of **1** yields a cation radical ($\text{V}_2^{\text{V,V}} \cdot+$, **2**) reactive towards CH_4 , while the catalytic cycle is fulfilled by additional electrochemical oxidation and cation radical regeneration.

Results

Discovery of ambient CH_4 activation with vanadium (V)-oxo catalyst. The d^0 vanadium (V)-oxo catalyst (**1**) was prepared by dissolving V_2O_5 in 98% H_2SO_4 . Cyclic voltammograms of 10 mM **1** in 98% H_2SO_4 under 1-bar nitrogen gas (N_2) (blue), 1-bar CH_4 (red), and a blank control (black) are displayed in Fig. 2a at 25 °C on a platinum (Pt) working electrode. A quasi-reversible peak corresponding to $\text{V}^{\text{V}}/\text{V}^{\text{IV}}$ redox couple was observed with a midpoint potential $E_{1/2} = 0.644$ V vs. $\text{Hg}_2\text{SO}_4/\text{Hg}$ reference electrode, with a diffusion coefficient $D = 2.18 \times 10^{-11} \text{ m}^2 \text{ s}^{-1}$ for **1** based on Randles–Savcik analysis (Supplementary Fig. 1a, b)²². Additional oxidation current of **1** was observed at the electrochemical potential $E > 1.6$ V vs. $\text{Hg}_2\text{SO}_4/\text{Hg}$, and such an oxidation current is larger in CH_4 than in N_2 . This observation suggests that **1** can be further oxidized electrochemically and CH_4 is likely to react with the resultant oxidized species. Bulk electrolysis in 98% H_2SO_4 under 1-bar CH_4 was conducted at a $E = 2.255$ V vs. $\text{Hg}_2\text{SO}_4/\text{Hg}$ for 6 h with an electrode of fluorine-doped tin oxide (Supplementary Fig. 1c). The liquid composition after electrolysis were analyzed by ^1H and ^{13}C nuclear magnetic resonance (NMR) spectroscopy. $\text{CH}_3\text{OSO}_3\text{H}$, which yields methanol after hydrolysis¹¹, was observed at chemical shift $\delta = 3.34$ ppm in ^1H NMR after electrolysis with 10 mM **1** under CH_4 (red in Fig. 2b). No gaseous or liquid products other than $\text{CH}_3\text{OSO}_3\text{H}$ were observed as a product of CH_4 oxidation within our detection limit via NMR spectroscopy (Fig. 2b), mass spectroscopy (Supplementary Fig. 2a, b) and gas chromatography (Supplementary Fig. 3). Organic products were not detected in the absence of **1** under CH_4 (black), with 10 mM **1** under N_2 (blue in Fig. 2b), or at a less anodic potential ($E = 1.855$ V vs. $\text{Hg}_2\text{SO}_4/\text{Hg}$) (Supplementary Fig. 2d). These data confirm that CH_4 undergoes a two-electron oxidation into $\text{CH}_3\text{OSO}_3\text{H}$, initiated by the electrochemical oxidation of **1**. The absence of a well-defined redox wave preceding the current onset in Fig. 2a suggests either a homogenous electrocatalysis limited by the rate of electron transfer or the occurrence of materials deposition during the scans of cyclic voltammetry. The measurement of X-ray photoelectron spectra on a FTO electrode after 6-h electrolysis with 10 mM **1** detected no residual V signal on the electrode (Supplementary Fig. 4) despite the observed $\text{CH}_3\text{OSO}_3\text{H}$ formation (1-bar CH_4 , $E = 2.255$ V vs. $\text{Hg}_2\text{SO}_4/\text{Hg}$). Reusing this vanadium-exposed FTO electrode for 6-h electrolysis in neat 98% H_2SO_4 under CH_4 yielded no CH_4 activation. These results suggest a likely homogenous electrocatalysis limited by charge transfer. We also conducted isotope-labeling experiments by introducing ^{13}C as the substrate at 1-bar pressure. The introduction of ^{13}C in lieu of CH_4 of natural abundance leads to the surge of ^{13}C signal at $\delta = 58.6$ ppm in ^{13}C NMR after electrolysis (Fig. 2c). An introduction of a 50% ^{13}C -enriched CH_4 yields not only the same peak in ^{13}C NMR but also a triplet in ^1H NMR with ^{13}C - ^1H doublet and ^{12}C - ^1H singlet at a 1:1 ratio of integration area (Supplementary Fig. 5). The optical absorption spectra of the solution before and after electrolysis were identical to each other (Supplementary Fig. 2e), implying that **1** as a catalyst was regenerated after electrolysis.

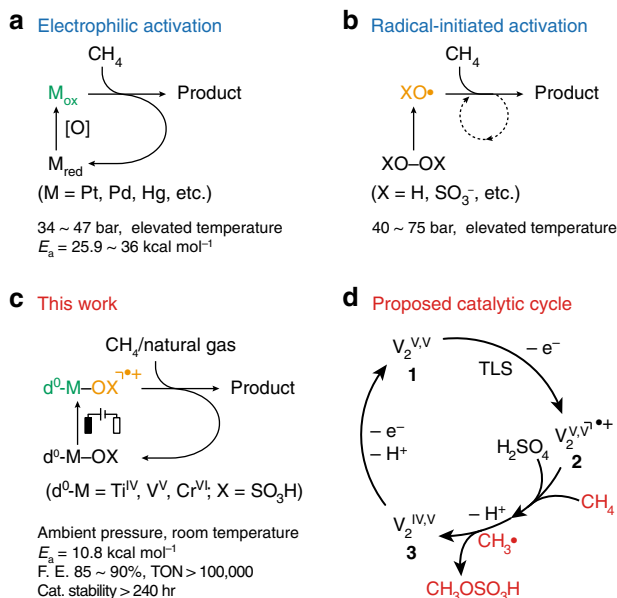


Fig. 1 Pathways to CH_4 functionalization. **a–c** Representative approaches of CH_4 functionalization based on electrophilic activation^{3–6} (**a**) and radical chain mechanism^{8–10} (**b**), in comparison with the proposed electrocatalytic method (**c**). **d** The proposed catalytic cycle of electrocatalytic CH_4 activation with d^0 vanadium (V)-oxo dimer (**1**). M_{red} and M_{ox} , reduced and oxidized metal active sites, respectively; $[\text{O}]$, chemical or electrochemical oxidation; E_a , activation energy; $d^0\text{-M}$, d^0 early transition metal species; F.E. Faradaic efficiency, TON turnover number, TLS turnover-limiting step.

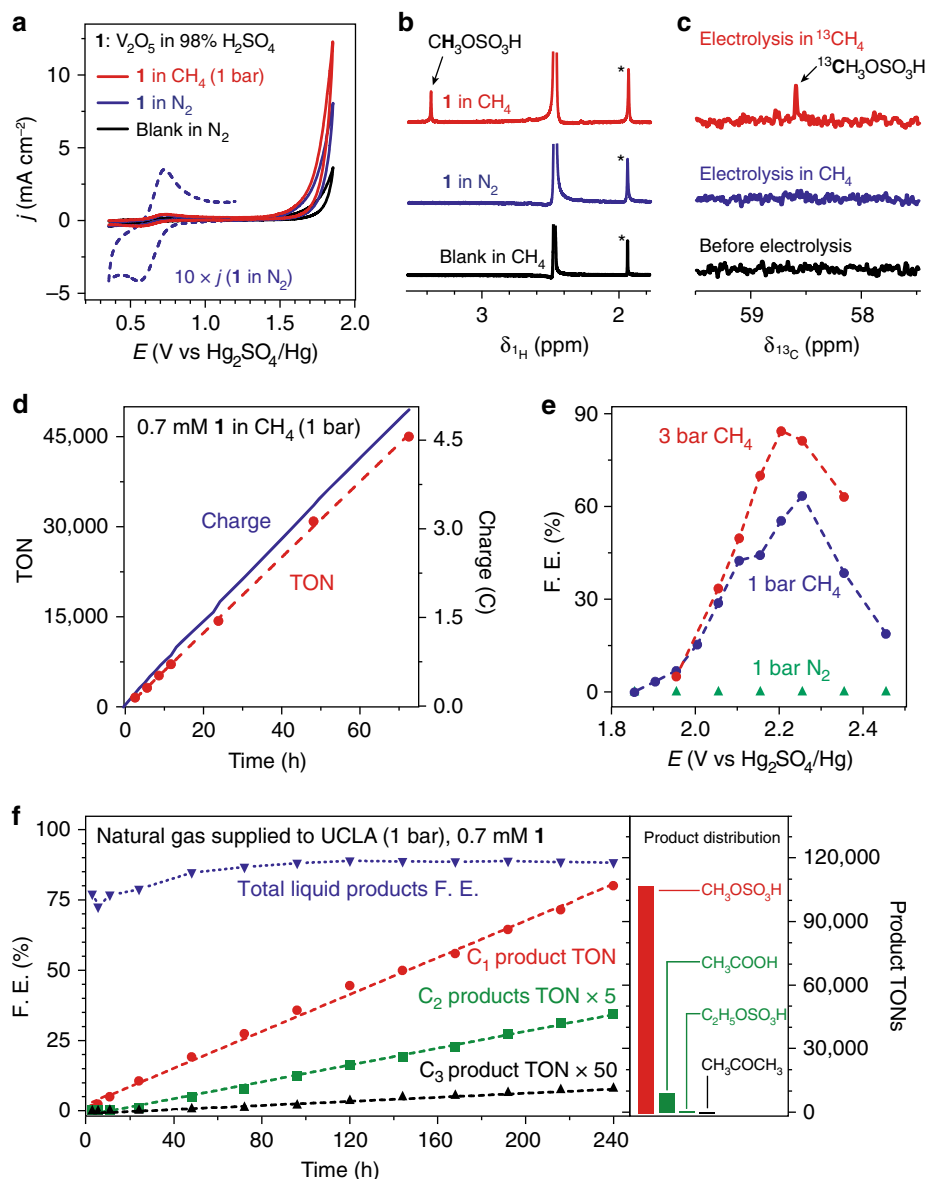


Fig. 2 Electrochemical functionalization of CH_4 and natural gas mixture. **a, b** Cyclic voltammograms (**a**) and ^1H NMR spectra of liquid samples after 6-h electrolysis (**b**) for 10 mM **1** in 1-bar CH_4 (red), 10 mM **1** in 1-bar N_2 (blue), and blanks without **1** (black). Dashed blue, current density (j) of blue trace magnified by a factor of 10. *, internal standard acetic acid. **c** ^{13}C NMR spectra of samples before (black) and after electrolysis with $^{13}\text{CH}_4$ (red) and CH_4 of natural abundance (blue), respectively. **d** Calculated TONs (red) and electric charges passed (blue) versus the duration of electrolysis. **e** F.E. of CH_4 functionalization in 10 mM **1** vs. electrode potential E under 1-bar N_2 (green), 1-bar CH_4 (blue) and 3-bar CH_4 (red). **f** Cumulative TONs for C_1 (red), C_2 (green, multiplied by a factor of 5), and C_3 products (black, multiplied by a factor of 50) as well as F.E. values of total liquid products (blue) are plotted against the duration of bulk electrolysis. TON values for $\text{CH}_3\text{OSO}_3\text{H}$ (red), CH_3COOH plus $\text{C}_2\text{H}_5\text{OSO}_3\text{H}$ (green), and CH_3COCH_3 (black) within 240 h are shown on the right, respectively. Natural gas mixture supplied by SoCalGas was used as the substrate at ambient pressure. Trace products beyond C_3 were also observed. 100 mV s^{-1} and Pt working electrode in (**a**); FTO working electrode in (**b**) to (**f**), and $E = 2.255\text{ V vs. Hg}_2\text{SO}_4/\text{Hg}$ in (**b**) to (**d**), and (**f**).

Electrochemical CH_4 and natural gas functionalization. The electrocatalysis with **1** is durable and selective for functionalization of CH_4 with high turnover numbers (TONs) and turnover frequencies (TOFs). Bulk electrolysis was conducted with 0.7 mM **1** at 25 °C under 1-bar pressure of CH_4 . Liquid aliquots at different time points were analyzed, and the electrochemical TONs were calculated based on the existing method^{19,23}. Figure 2d displayed the amount of electric charge and the calculated TONs as a function of electrolysis duration. A linear correlation suggests a durable catalyst of TON up to 45,000 in 72 h without signs of catalyst degradation. We also investigated the Faradaic efficiency (F.E.), defined as the selectivity of converting CH_4 into $\text{CH}_3\text{O}-\text{SO}_3\text{H}$ based on the amount of electric charge, as function of E at

25 °C. In 10 mM **1** (Fig. 2e), the absence of CH_4 leads to no product formation (green), and under 1-bar CH_4 an optimal F.E. = 63.5% when $E = 2.255\text{ V vs. Hg}_2\text{SO}_4/\text{Hg}$ (blue). We found that the reaction selectivity is limited by the mass transport and a limited solubility of CH_4 in solvent (~1 mM)¹¹. When CH_4 pressure increased to 3 bar, the optimal F.E. = 84.5% at $E = 2.205\text{ V vs. Hg}_2\text{SO}_4/\text{Hg}$ (red in Fig. 2e). The corresponding TOFs of **1** as an electrocatalyst are 483 and 1336 h^{-1} for CH_4 at 1 and 3-bar pressures, respectively, which are conservative and underestimated given the nature of our analysis (Supplementary Note 1). The measured TOF values at room temperature compare quite favorably with other reported catalysts at elevated temperatures and high pressures (Supplementary Table 1).

We expanded the substrate scope from CH₄ to ethane (C₂H₆), propane (C₃H₈), and ultimately natural gas mixture at 1-bar pressure. C₂H₆ was oxidized to a mixture of acetic acid (CH₃COOH) and ethyl bisulfate (C₂H₅OSO₃H) (Supplementary Fig. 6a), whose TOF values are 297 and 235 h⁻¹, respectively. C₃H₈ was converted to mostly isopropyl bisulfate (*i*-C₃H₇OSO₃H) with trace acetone (CH₃COCH₃) in a 6-h electrolysis (Supplementary Fig. 6b), with TOF values of 962 and 2 h⁻¹, respectively. One challenge in designing a process of natural gas utilization is to balance the low reactivity of the major component CH₄ with the high reactivity of minor light alkane components²⁴, as in some cases the latter substrates can react 100-time faster than CH₄²⁵. The similar TOF values among CH₄, C₂H₆, and C₃H₈ reported here renders **1** a suitable candidate of direct natural gas utilization at ambient conditions without much upstream separation.

Natural gas supplied to UCLA via pipeline by SoCalGas²⁶ was used as the substrate of electrolysis ($E = 2.255$ V vs. Hg₂SO₄/Hg) with 0.7 mM **1** in 98% H₂SO₄ at room temperature and ambient pressure. Powered by electricity, natural gas was oxidized into organic chemicals while dioxygen in air was reduced on the counter electrode, fulfilling a partial oxidation of natural gas with air with a net reaction of CH₄ + 1/2O₂ + H₂SO₄ → CH₃OSO₃H + H₂O. The yielded products mainly consist of CH₃OSO₃H from CH₄, CH₃COOH, and C₂H₅OSO₃H from C₂H₆, and CH₃COCH₃ from C₃H₈ in the natural gas. The TONs of C₁–C₃ products reached about 107,000, 9300, and 200 within 240 h, respectively (Fig. 2f) with the final concentration of CH₃OSO₃H approaching 10 mM (Supplementary Fig. 7). The observed one-order-of-magnitude difference between **1** and CH₃OSO₃H product again supports the catalytic feature of our observation. The total F.E. of all liquid products remain stable at around 90% during electrolysis after an initial induction period (Fig. 2f, Supplementary Table 2). The linear relationship between TONs and electrolysis durations suggest that **1** remains active and is tolerant to the impurities in natural gas mixture. Previous analysis suggests that a lower H₂SO₄ concentration in the electrolyte, ideally below 80%, is needed for industrial implementation¹¹. This requirement is against the thermodynamic limit of reactions in H₂SO₄ with SO₃ as the oxidant¹¹. Yet we found that **1** remains active towards CH₄ functionalization in aqueous solution with H₂SO₄ concentrations as low as 68% under 25 °C and 1-bar CH₄ (Supplementary Fig. 6c), yielding a mixture of methanol and CH₃OSO₃H (Supplementary Fig. 6d). The robustness under prolonged operation and the applicability in diluted H₂SO₄-H₂O mixed solvent renders the catalyst potentially suitable to be employed to functionalize natural gas with minimal maintenance.

Scale-up potential over vanadium (V)-oxo electrocatalyst. The reported catalyst **1** is also capable to yield high product concentrations amenable for practical implementations. Due to the limited solubility of CH₄ in the solvent within current batch reactor¹¹, electrocatalytic experiments of higher product concentrations were conducted under room temperature at 11-bar CH₄ pressure, in order to mitigate the mass transport issue of limited gas solubility (vide supra) (Supplementary Fig. 7). A 72-h electrolysis leads to a CH₃OSO₃H concentration of ~110 mM with F.E. = 81.2% ($E = 2.376$ V vs. Hg₂SO₄/Hg). Adding 1 M CH₃OSO₃H prior to the electrocatalysis under the same condition does not hinder the catalysis or decompose the pre-added CH₃OSO₃H. A single-pass conversion of 1% was observed in the mixed-flow electrochemical reactor, comparable to the results that lead to electrochemical reduction of CO₂ and CO at near-industrial level^{27,28}. The product concentrations reported here are higher than the ones in other electrocatalysis^{5,6}, and suggest that

high product concentration of electrocatalysis is attainable. There seems no observable fundamental limit for product concentrations exceeding one mole per liter, a threshold considered suitable for industrial applications¹¹.

Kinetics investigation of electrochemical CH₄ functionalization. The attractive feature of catalyst **1** led us to investigate the underlying mechanism during electrolysis with CH₄ as the substrate. The current density corresponding CH₃OSO₃H formation (j_{CH_4}), a surrogate of CH₄-activating rate, was investigated as a function of catalyst concentration [**1**] (Fig. 3a), the electrode potential E (Fig. 3b), the partial pressure of CH₄ (p_{CH_4}) (Fig. 3c), and the temperature T (Fig. 3d). A linear relationship with a slope = 1.03 ± 0.08 between $\log_{10}(j_{\text{CH}_4})$ and $\log_{10}([\mathbf{1}])$ suggests that CH₄ activation is first-order on **1** (Fig. 3a). When $\log_{10}(j_{\text{CH}_4})$ was plotted against E (Fig. 3b), a Tafel slope of about 120 mV dec⁻¹ was observed before j_{CH_4} plateaus at larger E values as CH₄ is depleted near electrode. This suggests that the first electron removal from **1** is the TLS, uncommon for homogeneous electrocatalysis (Supplementary Note 2). The overlapping points under 1 and 3-bar CH₄ pressure when $E < 2.1$ V vs. Hg₂SO₄/Hg suggest that CH₄ is not involved in the TLS or any pre-equilibrium steps. When $E > 2.1$ V vs. Hg₂SO₄/Hg, a linear relationship between $\log_{10}(j_{\text{CH}_4})$ and $\log_{10}(p_{\text{CH}_4})$ with a slope of 0.91 ± 0.07 (Fig. 3c) suggests that CH₄ is activated in a first order after the TLS. We also found that the residual current density, the difference between total current density (j_{total}) and j_{CH_4} , is independent of p_{CH_4} (Supplementary Fig. 2c). It further corroborates that no gaseous or liquid products other than CH₃OSO₃H were generated from CH₄ oxidation, and solvent oxidation into O₂ and possibly trace persulfate^{29,30} is the only plausible side reaction (vide infra). The Arrhenius plot between $\ln(j_{\text{CH}_4})$ and $1/T$ yields an apparent activation energy (E_a) as low as 10.8 ± 0.6 kcal mol⁻¹ (Fig. 3d), consistent with the observed ambient reactivity. When conducting electrolysis of **1** in 98% D₂SO₄ with CH₄ of natural isotope abundance, ²D and ¹H NMR spectra showed no H/D exchange in the methyl group of product CH₃OSO₃H (Supplementary Fig. 6e). This excludes the possible mechanism induced by an electrochemically generated superacid¹⁷, which should yield significant H/D exchange in the methyl group¹¹. In addition, when CH₄ was exposed to **1** in 98% H₂SO₄ with added K₂S₂O₈ or H₂O₂ in the absence of electricity, CH₄ functionalization was not observed at ambient conditions (Supplementary Fig. 6f). This illustrates that it is difficult for chemical method to sustainably generate reactive radical intermediates at room temperature, which necessitates our use of electrochemistry as proposed before. It also shows that the possible formation of peroxy species including peroxyacids is not contributing to the observed reactivity. When the electrolyte was switched from 98% H₂SO₄ to oleum with 20% SO₃, a 5.4:1 molar ratio between CH₃SO₃H and CH₃OSO₃H was observed after electrocatalysis (Supplementary Fig. 8). This indicates the formation of CH₃• radical during the catalysis, which yields CH₃SO₃H in the presence of SO₃⁹. Overall, our experimental data support an electrochemical catalysis of low activation energy. After a turnover-limiting one-electron oxidation of **1**, the oxidized species undergoes a first-order C–H activation in CH₄ and a formation of CH₃• radical (Fig. 1d).

Unveiling dimer structure of vanadium (V)-oxo catalyst. Despite its ease of preparation, the structural information of **1** is not well understood. It was hypothesized to be a V₂^{V,V} dimer with two terminal V^V≡O moieties connected by a bridging oxo²¹. We measured **1**'s optical absorption (Supplementary Fig. 9a) and the ⁵¹V NMR spectrum (Supplementary Fig. 9b), which confirmed that **1** is different from monometallic VO₂⁺ species in an

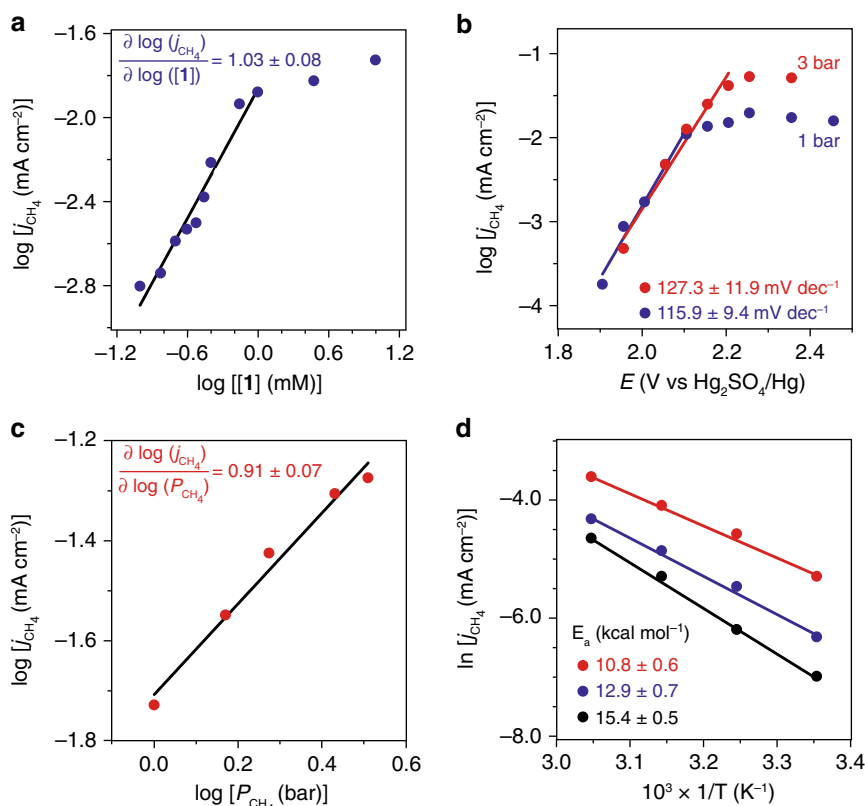


Fig. 3 Electrochemical kinetics. **a** The logarithmic of partial current density for CH₄ functionalization, $\log(j_{\text{CH}_4})$, versus the logarithmic of **1**'s concentration, $\log([\mathbf{1}])$. **b** $\log(j_{\text{CH}_4})$ vs. E under CH₄ pressures of 1 bar (blue) and 3 bar (red) with the fitted Tafel slopes displayed. **c** $\log(j_{\text{CH}_4})$ vs. the logarithmic of CH₄ pressure, $\log(p_{\text{CH}_4})$. **d** The natural logarithmic of partial current density for CH₄ functionalization, $\ln(j_{\text{CH}_4})$, vs. inverse of temperature, T^{-1} , at 1.955 V (black), 2.005 V (blue), and 2.055 V (red) vs. Hg₂SO₄/Hg, respectively. The corresponding apparent activation energies (E_a) are displayed. Unless noted specifically, 25 °C, 10 mM **1** in 98% H₂SO₄, $E = 2.255$ V vs. Hg₂SO₄/Hg, $p_{\text{CH}_4} = 1$ bar, data recorded from 6-h bulk electrolysis.

aqueous medium Density functional theory (DFT) calculations suggest that **1** may exist as two isomers, **1a** and **1b** (Fig. 4a), with a calculated energy difference of 1.2 kcal mol⁻¹. In an attempt to obtain the correct structure of **1** and real conformation in solution, X-ray absorption spectroscopy of V atom was conducted for 10 mM **1** in 98% H₂SO₄, solid V₂O₅, and metallic V foil (solid red, dashed blue, and dashed yellow in Fig. 4b, c, respectively). We carried out a least-square-regression analysis on X-ray absorption near-edge structure (XANES) for the threshold positions, the first peak in the derivative spectra, of VO, V₂O₃, VO₂, and V₂O₅ to determine the electronic structure and oxidation state of vanadium in **1** (Supplementary Fig. 9c)³¹. The electronic structure of vanadium in **1** remains similar to that of vanadium in V₂O₅, confirming the d⁰ electronic structure of vanadium. The extended X-ray absorption fine structure (EXAFS) can offer coordination information of absorbing atoms by extracting the structural parameters. As shown in Fig. 4c, the absence of noticeable peaks in the region beyond 4 Å (solid red), compared with those of V₂O₅ and V foil (dashed blue and dashed yellow, respectively), indicates that **1** is a complex homogeneously dispersed in the solvent. The peak around 1.56 Å in **1**'s EXAFS spectrum (gray area) is attributed to the V–O bonds, following the assignment of V–O bonds in the V₂O₅ sample. While this comparison provides some information, the general low symmetries of the vanadium-based species prevent us from gaining detailed structural information of **1** solely based on EXAFS data³². To this end, we conducted the fitting of **1**'s V K-edge EXAFS spectrum combining the structure suggested by DFT calculations (shown in Fig. 4d). It reveals that the central V atoms are penta-coordinated by O atoms with three types of V–O bond lengths (1.58, 1.68, and 1.96 Å) in the first coordinated

shell, with a bridging oxo with a V–O bond length of 1.68 Å. We note that the EXAFS of **1** suggests a unique coordination environment 2.0–3.5 Å away from V atom (blue area), which is different from the monometallic VO₂⁺ species in aqueous medium (Supplementary Fig. 9d). The fitting results of second shell (blue area) indicate that consistent with the predicted structure **1a**, there are not only three S atoms in the second shell (2.73 and 3.13 Å) but also one V atom at the distance of 3.27 Å away from the central V atom (Supplementary Table 3). Detailed analysis is provided in the Supplementary information (Supplementary Fig. 9e, f). These results reveal the existence of a hypothesized structure of μ -oxo bridged V₂^{V,V} dimer³³, and suggest that **1a** is the structure of **1** in the solution.

Operando characterizations for mechanistic study. Additional operando characterizations were conducted to confirm a homogeneous electrocatalysis and elucidate identities of immediate species. Operando Raman spectroscopy measures the vibrational spectra of chemical species near the FTO electrode at different values of E in CH₄. No spectral changes were observed and the vibrational spectra evidently differs from solid V₂O₅ sample (Supplementary Fig. 10). This suggests that there is no detectable heterogeneous intermediate deposited on the FTO electrode during electrocatalysis. Operando XAS spectra of V atom was also measured at different values of E in CH₄. Largely, the XANES and EXAFS spectra (Supplementary Figs. 11 and 12) differ from the ones of solid V₂O₅ sample and supports a homogeneous electrocatalysis. Yet some information of reaction intermediates is available. The formal oxidation state of V species, indicative in

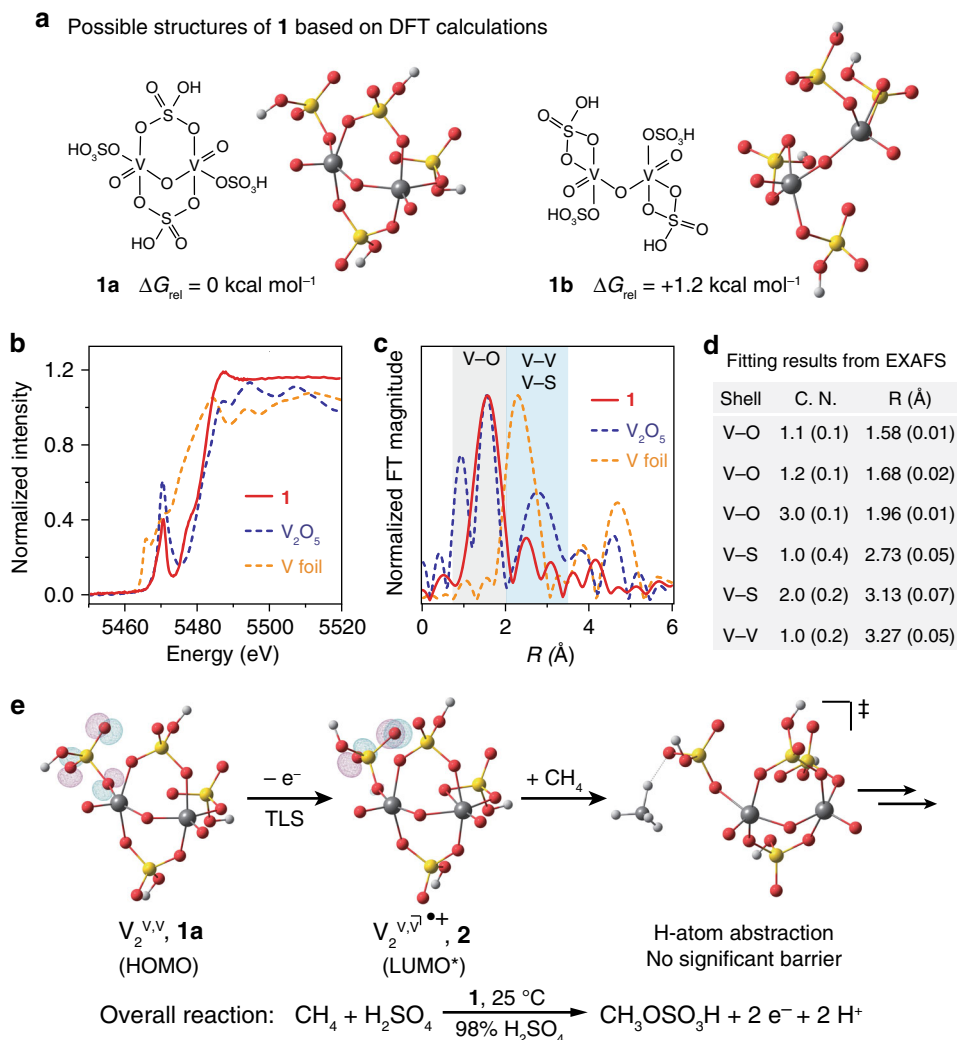


Fig. 4 Structural information of the catalyst and a proposed mechanism. **a** Possible isomeric structures of **1** and their relative energetics based on DFT calculations. **b**, **c** Normalized intensity of V K-edge X-ray absorption near-edge structure (XANES) (**b**) and extended X-ray absorption fine structure (EXAFS) (**c**) for **1** (solid red), V_2O_5 (dashed blue), and metallic V (dashed yellow). **d** Calculated coordination number (C.N.) and the distance (R) away from V atom based on EXAFS results. **e** Calculated frontier orbitals involved in the TLS and the proposed transition state of C-H activation step. HOMO highest occupied molecular orbital, LUMO lowest unoccupied molecular orbital. *Designated when considering spin-orbital coupling, equivalent to singly occupied molecular orbital (SOMO) in restricted formalism.

the pre-edge region of XANES spectra (Supplementary Fig. 11), decreases from +5 to near +4 with increasing value of E , contrary to the typical trend observed in heterogeneous catalysts of electrochemical oxidation³⁴. This reveals the presence of mixed-valence $\text{V}_2^{\text{IV,V}}$ during catalysis (Supplementary Note 3). It also supports a homogenous, diffusion-controlled catalysis, since a hypothetical immobile V(IV) species deposited on the electrode may not have long enough lifetime to be detectable (Supplementary Note 3), given the large thermodynamic driving force of oxidizing V(IV) (>1.2 V from Fig. 2a). The pre-edge region also witnesses a broadening and intensity decrease of the pre-edge peak concurrent with the increase of E and the observation of electrocatalytic CH_4 functionalization (Supplementary Fig. 11). This suggests an increase of coordination symmetry near V atom and possibly a loss of sulfonic ligand³¹. The operando EXAFS results (Supplementary Fig. 12) also displays a decrease of average coordination number of sulfonic ligands per V atom concurrent with increasing E values. Those results imply that the bisulfate group in $\text{CH}_3\text{OSO}_3\text{H}$ likely originate from the vanadium catalyst, a plausible radical rebound mechanism³⁵.

Proposed electrocatalytic cycle with vanadium (V)-oxo dimer.

Combining experimental and computational results, we established a proposed catalytic cycle of **1** for CH_4 functionalization (Fig. 1d) despite its uncommon assignment of TLS that warrants additional investigation (Supplementary Note 2). A turnover-limiting electrochemical oxidation of **1a** removes one electron from O 2p orbitals in the sulfonic ligand, which is calculated as the highest occupied molecular orbital (HOMO) of **1a** (Fig. 4e). The resultant cation radical **2** is predicted to possess an empty frontier spin-orbital on the same O 2p orbitals (lowest unoccupied molecular orbital (LUMO) of **2** in Fig. 4e), which is postulated to initiate H-atom abstraction from CH_4 . DFT calculations predict reaction trajectory between **2** and CH_4 without significant energy barrier (Fig. 4e, Supplementary Fig. 13a). This is consistent with our experimental observation that the TLS is the one-electron oxidation of **1** other than the step of C-H activation (Supplementary Note 2). The calculated barrier-less C-H activation also helps explain the similar TOFs toward various light alkanes in the natural gas²⁴. Currently, we were unable to experimentally characterize

2 and the H-atom abstraction step due to its transient nature, which will be of our research focus in the future. Yet the subsequent steps of CH₄ functionalization seems to proceed with the formation of CH₃• and a radical rebound process³⁵. This leads to a two-electron oxidation and CH₃OSO₃H formation with a ligand loss on a V₂^{IV,V} dimer (3), which will be readily re-oxidized electrochemically to regenerate 1 (Fig. 1d, Supplementary Fig. 14).

Exploration of molecular and material variants for vanadium (V)-oxo catalyst. DFT calculations of the atomic charges³⁶ suggest that cation radical 2 is stabilized thanks to orbital delocalization, in comparison to the scenario when one electron was removed from sulfuric acid (Supplementary Fig. 13b, c). This is consistent with the results that the calculated ionization energies of 1a is lower by 12–14 kcal mol⁻¹ than that of sulfuric acid. This implies that the metal-oxo centers as carrier of sulfonic ligands stabilize the electrochemically generated cation radical, at the same time maintain a cation radical reactive enough for ambient CH₄ functionalization. Other d⁰ early transition-metal-oxo species can possess similar reactivities. We found that d⁰ metal-oxo species, including Ti^{IV}-oxo and Cr^{VI}-oxo, are also electrochemically active towards functionalizing CH₄ at ambient conditions (Supplementary Fig. 15). A more extensive survey over the first half of the Period 4 elements except Sc indicates that only Ti, V, Cr, and possibly Mn display similar reactivities (Supplementary Fig. 16). It suggests the strategy of employing d⁰ early transition-metal-oxo species is generally applicable for ambient electrochemical functionalization of natural gas. As such a general trend of reactivity was not observed before, we posit our electrochemical approach may offer new perspective towards the challenge of CH₄ functionalization.

Practically, a heterogeneous catalyst variant may also be desirable. While 1 is characterized as a homogenous catalyst, we found a two-dimensional layered material, VOPO₄·2H₂O (4) with exposed V-oxo edges³⁷ (Supplementary Fig. 17a, b), acts as a heterogeneous variant of 1 in 98% H₂SO₄ (Supplementary Fig. 17c, d). This preliminary result suggests that even within the same metal-oxo system, the catalyst subsequently its reactivity can be tuned with additional materials design and engineering. This heterogeneous variant also simplifies product separation in downstream process, thanks to the absence of vanadium in the liquid phase.

Discussion

Overall, the general tunability of catalyst composition may herald better catalysts with higher TOF, lower oxidation potential, as well as versatile design of the overall process. The ambient condition of reported catalysis facilitates the use of O₂ in ambient air as the terminal electron acceptor, as well as the use of ambient natural gas feedstock for onsite functionalization without a centralized facility. Future research will focus on possible scale-up with the exploration of optimal reaction conditions. The employment of 98% H₂SO₄ or more diluted acids, other than oleum, mitigates the generation of excessive acid in product separation and is attractive for practical application³⁸. Additional fundamental and engineering investigation, including the employment of gas diffusion electrode³⁹ as well as ingenious design of electrochemical reactors²⁸, will further explore the possible application of converting CH₄ into commodity chemicals with minimal infrastructure support at remote locations. This will lead to the more efficient usage of green-house gases and reducing their emission into atmosphere.

Methods

Chemicals and materials. All chemicals were purchased from Sigma-Aldrich, Thermo Fisher Chemical, or VWR International, unless otherwise stated. All chemicals were used as received unless specified. Dimethyl sulfoxide-d₆ (DMSO-d₆) was purchased from Cambridge Isotope Laboratories, Inc. All deionized (DI) water was obtained from a Millipore Milli-Q Water Purification System. Fluorine-doped Tin Oxide (FTO) glass was purchased from Hartford Glass Incorporation. CH₄ (99.5%) was purchased from Airgas, C₂H₆ (99%), C₃H₈ (98%), and ¹³CH₄ (99%; 99 atom% ¹³C) were purchased from the Sigma-Aldrich. Natural gas mixture was obtained from the outlet in Molecular Science Building 4211, Department of Chemistry and Biochemistry, UCLA, which is supplied via pipeline by SoCalGas. SRI multiple gas analyzer #5 gas chromatograph (GC), 8610C is used to analyze the natural gas mixture. The components are 91.78 mole% CH₄, 4.31 mole% C₂H₆, 0.31 mole% C₃H₈, 0.04 mole% *n*-C₄H₁₀, 0.03 mole% *i*-C₄H₁₀, 0.01 mole% *n*-C₅H₁₂, 0.01 mole% *i*-C₅H₁₂, and 0.81 mole% CO₂. Unless specifically noted, reagent-grade 98% H₂SO₄ (VWR BDH3074-3.8LP) was employed as the solvent, which contains 5 ppm of metal impurities. When needed, we also employ high-purity 98% H₂SO₄ (Sigma-Aldrich 339741), which contains 0.3 ppm of metal impurities as shown in the product certificate.

Chemical and material characterizations. Ultraviolet–visible (UV–vis) spectra was conducted on Hewlett-Packard 8453 UV–vis spectrophotometer. Proton NMR (¹H-NMR) and carbon NMR (¹³C-NMR) were recorded on a Bruker AV400 (400 MHz) spectrometer. Deuterium NMR (²D-NMR) was recorded on a Bruker AV500 (500 MHz) spectrometer. Vanadium NMR (⁵¹V-NMR) was performed on an Agilent DD2 600 (600 MHz) spectrometer. Powder X-ray diffraction (XRD) patterns were measured on a Panalytical X'Pert Pro X-ray Powder Diffractometer with a Cu Kα source (λ = 1.54178 Å). The intensities were recorded within the 2θ range from 10° to 60° with a voltage of 45 kV, and a current of 40 mA. Scanning electron microscope image was measured with a JEOL JSM 6700F instrument. XANES and EXAFS were recorded at BL17C of National Synchrotron Radiation Research Center (NSRRC), Hsinchu, Taiwan. Gas chromatography–mass spectrometry (GC-MS) was performed on Agilent 6890-5975 GC-MS with Inert XL Selective Detector. The GC is equipped with a capillary HP-5MS column (Model No.: 19091S-433, 30.0 m × 250 μm × 0.25 μm). The instrument is operated with an oven temperature of 50 °C, an inlet temperature of 280 °C, and a flow rate of 1.2 mL min⁻¹ with helium carrier gas. A split/splitless injector is applied with a split ratio of 5:1 and a split flow of 5 mL min⁻¹. The MS has a source temperature of 230 °C and a quadrupole temperature of 150 °C. The SRI multiple gas analyzer #5 GC is equipped with 3 S.S. columns including 18" Hayesp D, 3"MS 5A and 6' Hayesp D. The instrument is operated with an oven temperature of 50 °C, a temperature profile from 50 to 270 °C, and a flow rate of 40 mL min⁻¹ at 15 psi with argon carrier gas. X-ray photoelectron spectroscopy (XPS) was measured on a Kratos AXIS Ultra spectrometer (Kratos Analytical, Manchester, UK).

Catalyst preparation. Homogeneous bimetallic catalyst 1 was prepared by dissolving vanadium pentoxide (V₂O₅) in 98% H₂SO₄ with ultra-sound treatment for 6 h. Homogeneous titanium (IV)-oxo and chromium (VI)-oxo catalysts were prepared by dissolved titanyl sulfate (TiOSO₄) and potassium chromate (K₂CrO₄) in 98% H₂SO₄, respectively. The heterogeneous variant 4 (VOPO₄·2H₂O) was prepared based on previous literature^{37,40}. V₂O₅ (4.8 g), H₃PO₄ (85.5%, 26.6 mL), and H₂O (115.4 mL) were refluxed at 110 °C for 16 h. After gently cooling down to room temperature, the yellow precipitate in the mixture was collected by filtration and washed several times with water and acetone. The resulting sample was dried in an oven at 100 °C for 3 h. When 4 was investigated for its electrochemical response, 4 was loaded onto a FTO electrode via a dip-coating procedure. A dispersion of 4 was prepared at a concentration of 6 mg mL⁻¹ in 2-propanol. The yellow dispersion was ultrasonicated for 30 min until the color of the dispersion became faded. Afterwards, sodium carboxymethyl cellulose (CMC) was added into the dispersion (weight ratio of VOPO₄·2H₂O: CMC = 80: 5). The mixture was stirred at 600 revolution per minute (rpm) on the heating plate to remove excess 2-propanol and form a homogenous slurry, which was then dip-coated onto FTO at a loading amount of 1.9 mg cm⁻² for 4.

Electrochemical characterization. All electrochemical experiments were recorded using a Gamry Instruments Reference 600+ and Interface 1000 potentiostats. Unless mentioned specifically, a three-electrode setup was applied with a Pt wire pseudo-reference electrode and a Pt counter electrode. The Pt pseudo-reference electrode was calibrated to a Hg₂SO₄/Hg (saturated K₂SO₄) reference electrode (CH Instrument, Inc.) via the measurement of open-circuit potentials. The relationship is $E(\text{V vs. Hg}_2\text{SO}_4/\text{Hg}) = E(\text{V vs. Pt}) + 0.755 \text{ V}$. The gas environment of the electrochemical cell was controlled either CH₄ (Airgas, 99.5%) or N₂ (Airgas, 99.999%), which were bubbled into the reactor at rates of 7.2 (CH₄) and 10 (N₂) standard cubic centimeters per minute (sccm) with the use of a mass flow controllers (Omega Engineering, Inc., FMA5510A). The data were reported after *iR* compensation. Unless noted specifically, the electrolyte is 98% H₂SO₄ with a certain vanadium concentration of 1.

Experiments of cyclic voltammetry were conducted in a single-chamber electrochemical cell with a 2-mm Pt working electrode (CH Instruments, Inc.). Bulk electrolysis with 5 mL homogeneous catalyst solution was typically conducted in a two-chamber electrochemical cell with a Nafion 117 membrane as the separator and a piece of commercial fluorine-doped tin-oxide (FTO) glass as the working electrode. Here, the FTO glass was encapsulated with Teflon tapes so that the exposed electrode is 1 × 1 cm in dimension. The solution was pre-saturated with CH₄ or N₂ for 20 min before the commencement of electrolysis. The background signal contribution of FTO glass was subtracted for the recorded data. Liquid aliquots were taken before, during and after the electrolysis for product analysis. Gaseous samples were taken manually from the outgas of the reactor, diluted with pure N₂ (1:5 ratio) for transportation purpose, and manually injected into the GC-MS. The injected permanent gas was not well separated by the column, but the MS spectra of the eluted gas peak (*t* ~3.3 min) was capable to quantify permanent gases with a detection limit of ~10 ppm. Additional measurements of gas chromatography for the gaseous effluents was conducted by the SRI multiple gas analyzer #5. The experiments at elevated pressure was conducted into a custom-designed setup utilizing a pressure vessel with two gas feedthrough and three electric feedthroughs (Parr Instrument, Series 4600, 1000 mL). In this setup, the gas pressure was controlled between 1 and 11 bar and a constant gas flow of up to 28.7 sccm was maintained during the electrolysis. The temperature of the electrolysis was maintained by an oil bath at a range between 25 and 55 °C. For experiments using substrates other than CH₄, the same procedure is followed except the gas flow rate is set at 10 sccm calibrated against N₂. In the 240-h electrolysis using natural gas mixture as the substrate, the electrolyte was refilled after each aliquot sampling in order to maintain a constant electrolyte volume. Experiment with 50% ¹³C-enriched CH₄ was conducted by feeding regular CH₄ and ¹³CH₄ gases at equal flow rates controlled by two mass flow controller.

We found that typical reagent-grade 98% H₂SO₄ possesses nonzero background activity toward CH₄ at high electrochemical potential (Supplementary Fig. 16). We argue that such background activity is due to the trace metal impurity, possibly V as H₂SO₄ is industrially synthesized by a V₂O₅ catalyst in the contact process. The reagent-grade 98% H₂SO₄ or oleum employed in most studies contains about 5 ppm of metal impurities (VWR BDH3074-3.8LP). When we employed high-purity 98% H₂SO₄ (Sigma-Aldrich 339741) that only contained 0.3 ppm of metal impurities as shown in the product certificate, the observed reactivity of neat 98% H₂SO₄ vanished (Supplementary Fig. 16).

When the heterogeneous variant **4** was investigated for its electrochemical response, a similar procedure was followed. However, owing to the difference of solution composition, the Pt pseudo-reference electrode has a different relationship with the Hg₂SO₄/Hg reference electrode: $E(\text{V vs. Hg}_2\text{SO}_4/\text{Hg}) = E(\text{V vs. Pt}) + 0.268 \text{ V}$.

Attempts of using chemical oxidants at ambient conditions. When CH₄ (7.2 sccm, 1 bar) was bubbled into a 98% H₂SO₄ solution with 10 mM **1** and 10 mM K₂S₂O₈ for 6 h at ambient conditions, the formation of methyl bisulfate (CH₃O-SO₃H) as a possible product of CH₄ oxidation was not observed (Supplementary Fig. 6f). Similar experiment was conducted with 10 mM H₂O₂ in lieu of K₂S₂O₈. The formation of methyl bisulfate (CH₃OSO₃H) as a possible product of CH₄ oxidation was not observed (Supplementary Fig. 6f), either.

Quantification of liquid products. ¹H-NMR was applied to quantify product accumulation in DMSO-*d*₆ using acetic acid (CH₃COOH) as the internal standard. Totally, 0.4 mL liquid aliquots from electrolysis were mixed with 0.1 mL DMSO-*d*₆ prior to the measurements. Chemical shifts are reported on a parts-per-million (ppm) scale. Methyl bisulfate (CH₃OSO₃H) exhibits a singlet at 3.34 ppm while the singlet from acetic acid (CH₃COOH) peak resides at 1.96 ppm. A calibration curve was constructed by determining the relative ratio of integrated area between the NMR peaks of CH₃OSO₃H and CH₃COOH. Product quantification of C₂H₆, C₃H₈, and natural gas mixture follows the same protocol, except for the quantification of CH₃COOH as a C₂ product from C₂H₆. The quantification of CH₃COOH as a C₂ product was fulfilled by adding a known concentration of CH₃OSO₃H as an internal standard in a separate ¹H-NMR measurement.

Calculation of FE. The F.E. of bulk electrolysis was calculated based on the following equation:

$$\text{F.E.} = \frac{nFC_{\text{product}}V_{\text{solution}}}{\text{Overall charge}} \times 100\%, \quad (1)$$

Here, *F* is the Faraday's constant, *C*_{product} is the concentration of product after bulk electrolysis, *V*_{solution} is the total electrolyte volume, and the overall charge is the total electric charges passed through the working electrode. The variable *n* in the equation is the number of electrons required in order to generate one product molecule by electrochemistry. *n* = 2 for the formation of methyl bisulfate (CH₃OSO₃H) from CH₄, *n* = 2 and 6 for the formation of ethyl bisulfate (C₂H₅OSO₃H) and acetic acid (CH₃COOH) from C₂H₆, respectively. *n* = 2 and 4 for the formation of isopropyl bisulfate (*i*-C₃H₇OSO₃H) and acetone (CH₃COCH₃) from C₃H₈, respectively.

Calculation of TOF and TON. In the following we provide the protocols that we calculate the TOFs and TONs for the reported data, based on the methods established in prior literature^{19,23}.

The diffusion coefficient for **1** (*D*) was determined from the cyclic voltammograms based on the Randles-Sevcik equation²²:

$$j_p = 0.4463nFC_{\text{cat}} \left(\frac{nFvD}{RT} \right)^{\frac{1}{2}}, \quad (2)$$

Here *j*_p is the peak current density of quasi-reversible redox couple, *n* is the number of electrons transferred in the redox event, *F* is the Faraday's constant, *C*_{cat} is **1**'s concentration, *v* is the scan rate, *R* is the gas constant, and *T* is the temperature of experiment. As derived from Supplementary Fig. 1a, b, *D* = 2.18 × 10⁻⁷ cm² s⁻¹ for species **1** in the electrolyte.

The observed TOF of bulk electrolysis was determined based on the following equation^{19,23}:

$$\text{TOF} = \left(\frac{j_{\text{product}}}{nFC_{\text{cat}}} \right)^2 \frac{1}{D}, \quad (3)$$

Here, *j*_{product} is the partial current density of product formation in bulk electrolysis, *n* is the number of electrons required to generate one product molecule, *F* is the Faraday's constant, *C*_{cat} is the concentration of catalyst **1**, *D* is the diffusion coefficient of catalyst (2.18 × 10⁻⁷ cm² s⁻¹ for species **1** as determined above).

Similarly, the TON of bulk electrolysis was determined based on the following equation^{19,23}:

$$\text{TON} = \frac{C_{\text{product}}V_{\text{solution}}}{AC_{\text{cat}}} \sqrt{\frac{\text{TOF}}{D}}. \quad (4)$$

Here, *C*_{product} is the product concentration after bulk electrolysis, *V*_{solution} is the total electrolyte volume, *A* is the electrode area, *C*_{cat} is the concentration of catalyst **1**, *D* is the diffusion coefficient of catalyst (2.18 × 10⁻⁷ cm² s⁻¹ for species **1** as determined above), and TOF is the TOF calculated based on above protocol.

On the condition of a homogenous process with molecular catalyst **1**, the diffusion coefficient extracted from the V(V)/V(IV) redox couple is a reasonable approximate of the real catalytic redox couple, the vanadium(V)-oxo dimer and its one-electron-deficient cation radical, because we are unable to characterize the cation radical due to its transient nature. Here, we offer a rough estimate of the relative uncertainty of such an approximation based on our proposed mechanism. The Stokes-Einstein relationship⁴¹ predicts that the diffusion coefficient *D* of similar molecules follows: *D* ~ MW^{-1/3}, in which MW is the molecular weight. As MW = 538.16 g mol⁻¹ for **1**, the relative uncertainty of *D* in our procedure is about 6% or 12%, assuming the loss of one or even two of the sulfonic ligands, respectively. As the TOF ~ *D*^{-1/2}, at most about 10% relatively uncertainty will incur in our practice.

Computational methods. All calculations were performed with Turbomole⁴²⁻⁵² using the M06 density functional⁵³. The def2-SVP basis set was used for geometry optimizations and free energy corrections, and the def2-TZVP basis set was used for electronic energies⁵⁴. Solvation was modeled with COSMO⁵⁵ with the dielectric constant set to 101⁵⁶. Images were rendered using Chemcraft⁵⁷. The natural bond orbital (NBO) analysis was used for atomic charge calculations⁵⁶.

Details of XAS experiments. XAS, including X-ray absorption near edge spectra (XANES) and extended X-ray absorption fine structure (EXAFS), at V K-edge were collected in total-fluorescence-yield mode at ambient conditions at BL17C of National Synchrotron Radiation Center (NSRRC), Hsinchu, Taiwan. Spectra were recorded in the energy range from -100 to 600 eV, relative to that of V K-edge absorption (5465.0 eV). The XAS spectra were processed by subtracting the baseline of pre-edge and normalizing that of post-edge. EXAFS analysis was carried out using Fourier transform on k³-weighted EXAFS oscillations to assess the contribution of each bond pair to Fourier transform peak. The curve fitting of EXAFS spectra was conducted using the software, REX2000, with FEFF program.

The operando XAS experiments at V K-edge were conducted under the same procedure at TPS beamline 44A of NSRRC, Hsinchu, Taiwan. A three-electrode arrangement was used during the operando measurements. The electrolyte was saturated with 1-bar CH₄, and the measurements were performed using an Autolab PGSTAT204 potentiostat (Metrohm Autolab) in a customized reactor.

Operando Raman characterization. A three-electrode setup in a home-made cell was adopted for Operando Raman spectroscopy and the electrochemical measurements. The measurements in a CH₄-saturated electrolyte were recorded using a Raman microscopy (UniNano UNIDRON) and an Autolab PGSTAT204 potentiostat (Metrohm Autolab). A laser of 633 nm with a spot size of ~1 μm² served as the excitation source, and the output power was 2.5 mW. A 50× objective lens was employed for operando measurements during electrolysis, while all results were obtained under an exposure duration of 3 s with the accumulation number of 60 times.

Data availability

The data that support the findings of this study are available from the corresponding author upon reasonable request. The source data underlying Figs. 2a, d–f, 3, and Supplementary Figs. 1a, b, 2c, 6c, 7, 9c, 11d, 13a, 15, 16, 17c, d are provided as Source Data file following the url: <https://doi.org/10.6084/m9.figshare.12525524>.

Received: 9 May 2020; Accepted: 1 July 2020;

Published online: 23 July 2020

References

- McFarland, E. Unconventional chemistry for unconventional natural gas. *Science* **338**, 340–342 (2012).
- Schüth, F. Making more from methane. *Science* **363**, 1282–1283 (2019).
- Periana, R. A. et al. A mercury-catalyzed, high-yield system for the oxidation of methane to methanol. *Science* **259**, 340–343 (1993).
- Periana, R. A. et al. Platinum catalysts for the high-yield oxidation of methane to a methanol derivative. *Science* **280**, 560–564 (1998).
- O'Reilly, M. E., Kim, R. S., Oh, S. & Surendranath, Y. Catalytic methane monofunctionalization by an electrogenerated high-valent Pd intermediate. *ACS Cent. Sci.* **3**, 1174–1179 (2017).
- Kim, R. S. & Surendranath, Y. Electrochemical reoxidation enables continuous methane-to-methanol catalysis with aqueous Pt salts. *ACS Cent. Sci.* **5**, 1179–1186 (2019).
- Shan, J. J., Li, M. W., Allard, L. F., Lee, S. S. & Flytzani-Stephanopoulos, M. Mild oxidation of methane to methanol or acetic acid on supported isolated rhodium catalysts. *Nature* **551**, 605–608 (2017).
- Mukhopadhyay, S. & Bell, A. T. A high-yield approach to the sulfonation of methane to methanesulfonic acid initiated by H₂O₂ and a metal chloride. *Angew. Chem. Int. Ed.* **42**, 2990–2993 (2003).
- Basickes, N., Hogan, T. E. & Sen, A. Radical-initiated functionalization of methane and ethane in fuming sulfuric acid. *J. Am. Chem. Soc.* **118**, 13111–13112 (1996).
- Nizova, G. V., SussFink, G. & Shulpin, G. B. Catalytic oxidation of methane to methyl hydroperoxide and other oxygenates under mild conditions. *Chem. Commun.* 397–398 (1997).
- Gunsalus, N. J. et al. Homogeneous functionalization of methane. *Chem. Rev.* **117**, 8521–8573 (2017).
- Shilov, A. E. & Shul'pin, G. B. Activation of C–H bonds by metal complexes. *Chem. Rev.* **97**, 2879–2932 (1997).
- Meng, X. G. et al. Direct methane conversion under mild condition by thermo-, electro-, or photocatalysis. *Chem* **5**, 2296–2325 (2019).
- Zimmermann, T., Soorholtz, M., Bilke, M. & Schüth, F. Selective methane oxidation catalyzed by platinum salts in oleum at turnover frequencies of large-scale industrial processes. *J. Am. Chem. Soc.* **138**, 12395–12400 (2016).
- Diaz-Urrutia, C. & Ott, T. Activation of methane to CH₃⁺: a selective industrial route to methanesulfonic acid. *Science* **363**, 1326–1329 (2019).
- Labinger, J. A. & Bercaw, J. E. Understanding and exploiting C–H bond activation. *Nature* **417**, 507–514 (2002).
- Olah, G. A. Electrophilic methane conversion. *Acc. Chem. Res.* **20**, 422–428 (1987).
- Shilov, A. E. & Shul'pin, G. B. *Activation and Catalytic Reactions of Saturated Hydrocarbons in the Presence of Metal Complexes*. (Springer, Dordrecht, 2000).
- Savéant, J. M. *Elements of Molecular and Biomolecular Electrochemistry. An Electrochemical Approach to Electron Transfer Chemistry*. (Wiley, New Jersey, 2006).
- Sauermann, N., Meyer, T. H., Qiu, Y. A. & Ackermann, L. Electrocatalytic C–H activation. *ACS Catal.* **8**, 7086–7103 (2018).
- Madic, C., Begun, G. M., Hahn, R. L., Launay, J. P. & Thiessen, W. E. Dimerization of aquadioxovanadium(V) ion in concentrated perchloric and sulfuric-acid media. *Inorg. Chem.* **23**, 469–476 (1984).
- Zanello, P. *Inorganic Electrochemistry: Theory, Practice and Application*. (Royal Society of Chemistry, London, 2003).
- Costentin, C., Drouet, S., Robert, M. & Saveant, J. M. Turnover numbers, turnover frequencies, and overpotential in molecular catalysis of electrochemical reactions. Cyclic voltammetry and preparative-scale electrolysis. *J. Am. Chem. Soc.* **134**, 11235–11242 (2012).
- Labinger, J. A. Selective alkane oxidation: hot and cold approaches to a hot problem. *J. Mol. Catal. A* **220**, 27–35 (2004).
- Konnick, M. M. et al. A mechanistic change results in 100 times faster CH functionalization for ethane versus methane by a homogeneous Pt catalyst. *J. Am. Chem. Soc.* **136**, 10085–10094 (2014).
- Natural Gas Safety Data Sheet by SoCalGas. <https://www.socalgas.com/documents/safety/safety-data-sheet-natural-gas.pdf>.
- Dinh, C. T., Li, Y. G. C. & Sargent, E. H. Boosting the single-pass conversion for renewable chemical electrosynthesis. *Joule* **3**, 13–15 (2019).
- Ripatti, D. S., Veltman, T. R. & Kanan, M. W. Carbon monoxide gas diffusion electrolysis that produces concentrated C₂ products with high single-pass conversion. *Joule* **3**, 240–256 (2019).
- Zhu, J., Hii, K. K. & Hellgardt, K. Toward a green generation of oxidant on demand: practical electrosynthesis of ammonium persulfate. *ACS Sustain. Chem. Eng.* **4**, 2027–2036 (2016).
- Radimer, K. J. & McCarthy, M. J. *Electrolytic Production of Sodium Persulfate*. USA patent US 4,144,144 (1979).
- Wong, J., Lytle, F. W., Messmer, R. P. & Maylotte, D. H. K-edge absorption-spectra of selected vanadium compounds. *Phys. Rev. B* **30**, 5596–5610 (1984).
- Bunker, G. *Introduction to XAFS: A Practical Guide to X-Ray Absorption Fine Structure Spectroscopy*. (Cambridge University Press, Cambridge, 2010).
- Yamada, S., Katayama, C., Tanaka, J. & Tanaka, M. Molecular structure of (u-oxo)bis[oxobis(8-quinolinolato)vanadium(V)]. *Inorg. Chem.* **23**, 253–255 (1984).
- Bai, L. C., Hsu, C. S., Alexander, D. T. L., Chen, H. M. & Hu, X. L. A cobalt-iron double-atom catalyst for the oxygen evolution reaction. *J. Am. Chem. Soc.* **141**, 14190–14199 (2019).
- Huang, X. Y. & Groves, J. T. Beyond ferryl-mediated hydroxylation: 40 years of the rebound mechanism and C–H activation. *J. Biol. Inorg. Chem.* **22**, 185–207 (2017).
- Reed, A. E., Weinstock, R. B. & Weinhold, F. Natural population analysis. *J. Chem. Phys.* **83**, 735–746 (1985).
- Wu, C. Z. et al. Two-dimensional vanadyl phosphate ultrathin nanosheets for high energy density and flexible pseudocapacitors. *Nat. Commun.* **4**, 2431 (2013).
- Michalkiewicz, B., Ziebro, J. & Tomaszewska, M. Preliminary investigation of low pressure membrane distillation of methyl bisulphate from its solutions in fuming sulphuric acid combined with hydrolysis to methanol. *J. Membr. Sci.* **286**, 223–227 (2006).
- Higgins, D., Hahn, C., Xiang, C. X., Jaramillo, T. F. & Weber, A. Z. Gas-diffusion electrodes for carbon dioxide reduction: a new paradigm. *ACS Energy Lett.* **4**, 317–324 (2019).
- Yamamoto, N., Hiyoshi, N. & Okuhara, T. Thin-layered sheets of VOHPO₄·0.5H₂O prepared from VOPO₄·2H₂O by intercalation-exfoliation-reduction in alcohol. *Chem. Mater.* **14**, 3882–3888 (2002).
- Young, M. E., Carroad, P. A. & Bell, R. L. Estimation of diffusion-coefficients of proteins. *Biotechnol. Bioeng.* **22**, 947–955 (1980).
- Ahrlrichs, R., Bar, M., Haser, M., Horn, H. & Kolmel, C. Electronic-structure calculations on workstation computers—the program system turbomole. *Chem. Phys. Lett.* **162**, 165–169 (1989).
- Haser, M. & Ahrlrichs, R. Improvements on the direct SCF method. *J. Comput. Chem.* **10**, 104–111 (1989).
- Treutler, O. & Ahrlrichs, R. Efficient molecular numerical-integration schemes. *J. Chem. Phys.* **102**, 346–354 (1995).
- Eichkorn, K., Weigend, F., Treutler, O. & Ahrlrichs, R. Auxiliary basis sets for main row atoms and transition metals and their use to approximate Coulomb potentials. *Theor. Chem. Acc.* **97**, 119–124 (1997).
- Eichkorn, K., Treutler, O., Ohm, H., Haser, M. & Ahrlrichs, R. Auxiliary basis-sets to approximate Coulomb potentials. *Chem. Phys. Lett.* **242**, 652–660 (1995).
- Weigend, F. Accurate Coulomb-fitting basis sets for H to Rn. *Phys. Chem. Chem. Phys.* **8**, 1057–1065 (2006).
- Sierka, M., Hogeckamp, A. & Ahrlrichs, R. Fast evaluation of the Coulomb potential for electron densities using multipole accelerated resolution of identity approximation. *J. Chem. Phys.* **118**, 9136–9148 (2003).
- Deglmann, P., May, K., Furche, F. & Ahrlrichs, R. Nuclear second analytical derivative calculations using auxiliary basis set expansions. *Chem. Phys. Lett.* **384**, 103–107 (2004).
- Arnim, M. V. & Ahrlrichs, R. Parallelization of density functional and RI-Coulomb approximation in turbomole. *J. Comp. Chem.* **19**, 1746–1757 (1998).
- von Arnim, M. & Ahrlrichs, R. Geometry optimization in generalized natural internal coordinates. *J. Chem. Phys.* **111**, 9183–9190 (1999).
- Ahrlrichs, R. Efficient evaluation of three-center two-electron integrals over Gaussian functions. *Phys. Chem. Chem. Phys.* **6**, 5119–5121 (2004).
- Zhao, Y. & Truhlar, D. G. The M06 suite of density functionals for main group thermochemistry, thermochemical kinetics, noncovalent interactions, excited states, and transition elements: two new functionals and systematic testing of four M06-class functionals and 12 other functionals. *Theor. Chem. Acc.* **120**, 215–241 (2008).
- Weigend, F. & Ahrlrichs, R. Balanced basis sets of split valence, triple zeta valence and quadruple zeta valence quality for H to Rn: Design and assessment of accuracy. *Phys. Chem. Chem. Phys.* **7**, 3297–3305 (2005).
- Klamt, A. & Schuurmann, G. Cosmo—a new approach to dielectric screening in solvents with explicit expressions for the screening energy and its gradient. *J. Chem. Soc. Perkin Trans. 2*, 799–805 (1993).
- Gillespie, R. J. & Cole, R. H. The dielectric constant of sulphuric acid. *Trans. Faraday Soc.* **52**, 1325–1331 (1956).

57. Chemcraft—graphical software for visualization of quantum chemistry computations. <https://www.chemcraftprog.com>.

Acknowledgements

J.A.I. is supported by a Eugene V. Cota-Robles fellowship. D.Y. thanks the visiting graduate student fellowship from the China Scholarship Council. H.M.C. acknowledges the Ministry of Science and Technology, Taiwan (Contract no. MOST 107-2628-M-002-015-RSP). A.N.A. acknowledges the NSF Career Award (CHE-1351968), and the XSEDE and the UCLA-IDRE cluster Hoffman2 for computational resources. C.L. acknowledges the NSF Award (CHE-1955836), startup fund from the University of California, Los Angeles and the financial support of the Jeffery and Helo Zink Endowed Professional Development Term Chair. We thank Lina Gao and Xueqian Kong for the measurement of ^{51}V NMR spectroscopy, Weilai Yu and the Molecular Materials Research Center of the Beckman Institute of the California Institute of Technology for the measurement of XPS, Paula Diaconescu, Hosea Nelson, and Alexander Spokoyny for helpful discussions.

Author contributions

C.L. supervised the project. J.D. conducted the majority of electrolysis experiments and assisted the initial experiment design. S.C.L. conducted the XAS and operando Raman experiments and analyzed the data under supervision of H.M.C. J.A.I. participated the initial experiment design and first reported the catalytic activities. J.A.I., D.X., G.C., and D.Y. participated in the catalyst characterization. J.F. performed the DFT calculations under the supervision of A.N.A. C.L., J.D., and S.C.L. analyzed the data and wrote the initial draft of paper. All the authors discussed the results and assisted during the paper preparation.

Competing interests

A provisional patent has been filed under the names of C.L., J.D., and J.A.I. (U.S. 62/890,271). Remaining authors declare no competing interests.

Additional information

Supplementary information is available for this paper at <https://doi.org/10.1038/s41467-020-17494-w>.

Correspondence and requests for materials should be addressed to H.M.C., A.N.A. or C.L.

Peer review information *Nature Communications* thanks Timo Ott and the other, anonymous, reviewer(s) for their contribution to the peer review of this work.

Reprints and permission information is available at <http://www.nature.com/reprints>

Publisher's note Springer Nature remains neutral with regard to jurisdictional claims in published maps and institutional affiliations.



Open Access This article is licensed under a Creative Commons Attribution 4.0 International License, which permits use, sharing, adaptation, distribution and reproduction in any medium or format, as long as you give appropriate credit to the original author(s) and the source, provide a link to the Creative Commons license, and indicate if changes were made. The images or other third party material in this article are included in the article's Creative Commons license, unless indicated otherwise in a credit line to the material. If material is not included in the article's Creative Commons license and your intended use is not permitted by statutory regulation or exceeds the permitted use, you will need to obtain permission directly from the copyright holder. To view a copy of this license, visit <http://creativecommons.org/licenses/by/4.0/>.

© The Author(s) 2020